Novel angular velocity estimation technique for plasma filaments

M. Lampert,[1, a)] A. Diallo,[1] and S.J. Zweben[1]
Princeton Plasma Physics Laboratory,
Princeton, NJ 08540, USA

(Dated: 8 December 2022)

Magnetic field aligned filaments such as blobs and edge localized mode (ELM) filaments carry significant amount of heat and particles to the plasma facing components and they decrease their lifetime. The dynamics of these filaments determine at least a part of the heat and particle loads. These dynamics can be characterized by their translation and rotation. In this paper we present an analysis method novel for fusion plasmas which can estimate the angular velocity of the filaments on frame-by-frame time resolution. After pre-processing, the frames are two-dimensional (2D) Fourier-transformed, then the resulting 2D Fourier magnitude spectra are transformed to log-polar coordinates, and finally the 2D cross-correlation coefficient function (CCCF) is calculated between the consecutive frames. The displacement of the CCCF's peak along the angular coordinate estimates the angle of rotation of the most intense structure in the frame. The proposed angular velocity estimation method is tested and validated for its accuracy and robustness by applying it to rotating Gaussian-structures. The method is also applied to gas-puff imaging measurements of filaments in NSTX (National Spherical Torus Experiment) plasmas.

I. INTRODUCTION

Filaments in fusion plasmas are structures elongated along the magnetic field lines with elevated density and temperature compared to the background plasma. They are poloidally localized at any toroidal angle and toroidally localized at any poloidal angle.[1] They are ubiquitous to the background scrape-off layer (SOL) turbulence where these intermittent structures are called blobs.[2] Filaments are also created during the edge localized mode (ELM) crashes as ELM filaments.[3] Filaments are responsible for a significant fraction of particle and heat transport to the plasma facing components (PFCs) where they are deposited and could even cause permanent damage.[4] Filaments lower the life expectancy of the PFCs in future fusion reactors like ITER (International Thermonuclear Experimental Reactor).[5] The dynamics of these filaments determine part of their heat and particle loads on the PFCs, thus, understanding their behavior is important for future fusion energy production.

Previously we have assessed the translational dynamics of the ELM filaments in Ref. 6 and presented the utilized spatial displacement estimation (SDE) method in Ref. 7. By studying the translational velocity of ELM filaments analytical models were established which could explain some aspects of the observations. By studying the rotation of ELM filaments, one could establish further analytical models for explaining their rotation behavior. These models could support numerical simulations of ELMs and blobs which could contribute to the development of novel ELM and heat flux mitigation techniques. This motivated the development of the presented analysis technique.

In this paper we present a novel method for characterizing the rotational dynamics of plasma filaments (see Fig. 1). The pre-processed frames are first two-dimensional (2D) fast Fourier transformed (FFT). Hereafter, the Fourier magnitude spectra (FMS) of the frames are calculated and transformed into log-polar coordinates. These steps are called Fourier-Mellin transformation[8]. Then the 2D cross-correlation coefficient function (CCCF) is calculated between the consecutive log-polar transformed FMSs. Finally, the angle of rotation and the expansion fraction can be estimated from the displacement of the CCCF's peak from the origin. The angular velocity is calculated by dividing the angle of rotation by the sampling time.

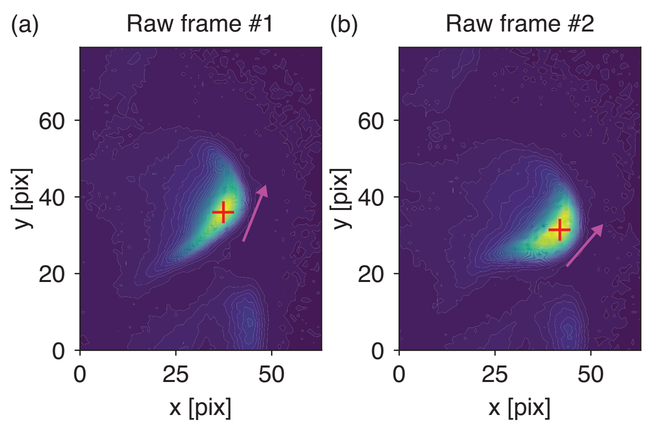

FIG. 1. Two consecutive frames of an example rotating structure from a GPI measurement of an ELM filament in shot No. #141319. (a) Raw frame at t=552.492 ms; (b) Consecutive raw frame at t=552.495 ms. The displacement of the structure is highlighted by the red crosses at the center of gravity of the structure. The magenta arrows point in the direction of the filament's characteristic angle and highlight the rotation.

The core of this Fourier-Mellin transformation-based method has been previously utilized in computer vision for image registration[9] and in biology research for tracking the movement of cells in samples[10]. In fusion research previously the angular velocity of blobs was typically estimated from identifying a characterizing contour path of the filament, fit-

[a)]The author to whom correspondence may be addressed: mlampert@pppl.gov

ting, e.g., an ellipse onto it, and calculating the angle from the fit[11]. However, structure-identification-based methods give noisy estimates for differential quantities like the angular velocity. The presented method is robust against noise and is computationally inexpensive. We have previously utilized the presented algorithm in our previous publication in Ref. 12, however, the details of the method were not discussed, and its accuracy was not assessed there either.

The development of the method was motivated by gas-puff imaging (GPI) measurements of spinning filaments; thus, this diagnostic is described here briefly. A more detailed description of GPI can be found in Refs. 13 and 14. In GPI measurements a puff of neutral gas (e.g., Deuterium or Helium) is injected into the SOL and edge plasma where the injected neutrals increase the line emission significantly. The emitted light is filtered to the wavelength of the line emission and is typically imaged with a fast camera. To measure the local plasma fluctuations in the poloidal-radial plane, the line of sight needs to be close to parallel to the magnetic field lines and perpendicular to the quasi-two-dimensional gas-puff. The gas-puff should be localized as much as possible to a two-dimensional (2D) plane perpendicular to the field lines. The measurement responses to electron fluctuations and negligibly to ion fluctuations.

The GPI measurements shown in this paper were performed on the NSTX (National Spherical Torus Experiment) spherical tokamak[15]. NSTX is a medium-sized, low-aspect ratio spherical tokamak with a major radius of $R = 0.85$ m and minor radius of $a = 0.67$ m ($R/a \geq 1.26$). The maximum toroidal field is $B_T = 0.6$ T. The plasma can be heated by NBI (Neutral Beam Injection) with up to 5 MW and by radio frequency heating with 6 MW.

The rest of the paper is organized as follows. Sec. II describes the steps of the angle rotation estimation method along with a brief description of the pre-processing steps, the Fourier-Mellin transform, and the 2D cross-correlation coefficient function. In Sec. III the method is tested by applying it on rotating and propagating Gaussian-shaped structures. In Sec. IV the introduced method is discussed by applying it to blob and ELM filament measurements, by comparing it to other angular velocity estimation methods, and by assessing its limitations and assumptions. Finally, Sec. V summarizes the results of the paper.

II. METHODOLOGY: ANGULAR VELOCITY ESTIMATION

This section presents the frame-by-frame angular velocity estimation method for plasma filament analysis. The method relies on the Fourier-Mellin transformation where the log-polar Fourier-magnitude spectra of consecutive frames are calculated after being pre-processed. Then the two-dimensional cross-correlation coefficient function (CCCF) is calculated between them. The shift of the CCCF's peak from the origin can be used to estimate the characteristic angle of rotation of a structure between the frames. The steps of the method are summarized in the flowchart in Fig. 2. The presented method can also estimate the so-called scaling factor which can be used to estimate the change of the characteristic structure size.

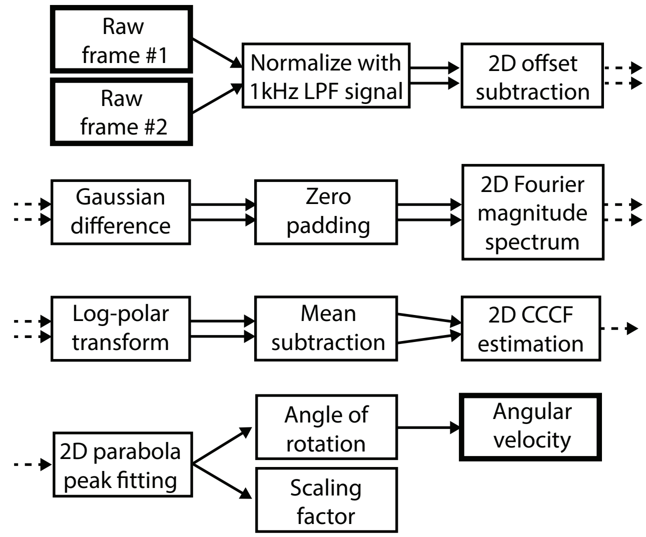

FIG. 2. Flowchart of the steps of the angular velocity estimation method.

A. Pre-processing

Before the presented analysis technique could be applied on the measurement data, a few diagnostic specific (time dependent background and polynomial offset subtraction) and analysis technique specific (difference-of-Gaussians) pre-processing steps need to be applied. The diagnostic dependent pre-processing steps are discussed in more detail in Ref. 7, here only a brief overview is given.

In fluctuation analysis it is necessary to separate the fluctuating and the background signal. In case of gas-puff imaging measurements of filaments in the scrape-off layer the fluctuating signal is originating from the intermittent filaments and the background signal is the response of the gas neutrals to the background plasma profiles. To remove the background from the raw signal the following technique is applied. The data is taken from the $[t_1 - 10\text{msec}, t_2 + 10\text{msec}]$ time range, where $[t_1, t_2]$ is the analyzed time range of the filaments. The data from this time range is filtered with a symmetric infinite impulse-response (IIR) filter[16] with a 1kHz elliptic kernel. The choice of the 10 ms time range extension corresponds to ten times the characteristic time of the filter kernel, i.e., $10/1\text{kHz} = 10\text{msec}$. This time range extension ensures that the edge effects of the filtering are completely suppressed in the analyzed time range. A 1kHz filter kernel was chosen because the background signal was found to be evolving on a 1 ms long time scale, while the investigated filaments were evolving on a $\sim 10\mu$s time scale. At the end the raw signal (see Fig. 3 (a)) was divided by the filtered signal to arrive at the background suppressed signal (see Fig. 3 (b)).

In different diagnostic setups the time scales of the background signal and the dynamics of the analyzed structures need to be at least a magnitude apart to prevent suppression of the analyzed phenomenon. Furthermore, the fluctuation-response of the background needs to be taken into consideration, as well. For example, in case of the GPI measurement, dividing the signal with the estimated response of the neutral gas was proved to be optimal, but in other measurements subtraction could be more efficient.

In the second pre-processing step (see Fig. 3 (c)) a two-dimensional polynomial is subtracted from each frame to remove the remaining background offset. The fit polynomial coefficients are found by least square fitting using the

$$\boldsymbol{c} = (\boldsymbol{X}^T\boldsymbol{X})^{-1}\boldsymbol{X}^T\boldsymbol{f'} \tag{1}$$

formula where c is the coefficient vector, $\boldsymbol{X}$ is the polynomial matrix and $\boldsymbol{f'}$ is the matrix of the pre-processed frame flattened to a vector. For the NSTX GPI signals, parabolic subtraction was found to be optimal. Further details of this 2D polynomial subtraction method can be found in Ref. 7.

In the last pre-processing step, the features of the structure are enhanced with a method called difference-of-Gaussians[17] (see Fig. 3 (d)). The raw frame is Gaussian blurred with a kernel having $\sigma = 1$pix standard deviation and it is subtracted from it. This step enhances features such as the boundary of a structure. This step is performed by an implementation in the scikit-image library[18].

B. Fourier-Mellin transform based rotation estimation

After pre-processing, the signal is Fourier-Mellin transformed. This transformation is the name for a collection of steps which includes fast-Fourier transformation, calculation of the Fourier magnitude spectra (FMS), and transforming it into log-polar coordinates, respectively. The applied method was implemented based on the work of Reddy et al[19]. In this current paper the details of the transformation are discussed as well as its application in fusion plasma analysis. Further details of the derivation are shown in the Appendix in Sec. A1.

1. Fourier-shift theorem

A straightforward estimation of the angular velocity would be to transform the consecutive frame pairs from Cartesian coordinates, (x,y), to polar coordinates, (r,ϕ), and then calculate the 2D spatial cross-correlation coefficient function (CCCF) between them similarly to the spatial displacement estimation[7]. Then one could estimate the angle difference from the displacement of the CCCF's maximum from the origin. However, this method would only work if the polar transformation was performed along the axis of rotation. Since the location of this axis is typically unknown in fusion plasma measurements, this simple estimation method breaks down. To tackle this issue, we implement a method which relies on the translation invariant 2D Fourier magnitude spectrum (FMS) of the frames rather than the frames themselves. This resolves the issue with the unknown rotation axis and renders the cross-correlation based rotation estimation feasible.

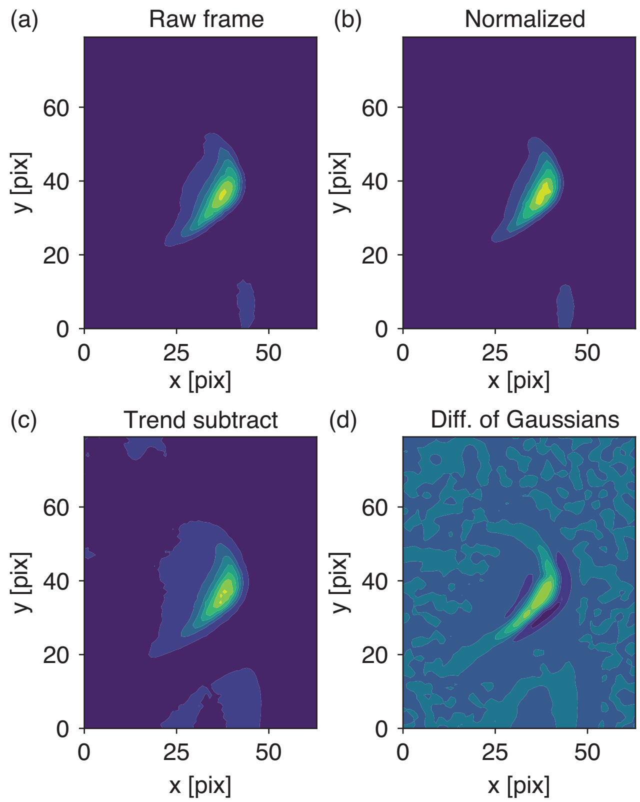

FIG. 3. Steps of the pre-processing: (a) Raw frame; (b) Background suppressed frame (raw frame divided by the 1kHz low-pass filtered signal); (c) Polynomial trend subtracted frame; (d) Feature enhancement after application of the difference-of-Gaussians filter.

It can be shown that linear displacement of a structure with (x_0, y_0) vector between two frames, f_1 and f_2, introduces only a constant phase shift between their 2D Fourier spectra, F_1 and F_2. Therefore, the magnitudes of their Fourier spectra, M_1 and M_2 are invariant to translation because the phase is cancelled. This is the Fourier-shift theorem and is expressed in

$$\begin{aligned} f_2(x,y) &= f_1(x-x_0, y-y_0) \\ F_2(\xi,\eta) &= e^{-2\pi j(\xi x_0+\eta y_0)} \cdot F_1(\xi,\eta) \\ M_2(\xi,\eta) &= M_1(\xi,\eta) \end{aligned} \tag{2}$$

.

2. Log-polar transformation

If rotation with angle θ_0, and linear scaling (expansion or contraction) with the scaling factor f_s in both x and y directions are introduced besides the linear translation with (x_0, y_0) between the frames, it can be shown (see Sec. A1) that their log-polar transformed FMSs are related to each other by

$$M_1(log(\rho),\theta) = M_2(log(\rho) - log(f_s), \theta - \theta_0) \qquad (3)$$

,

where $(\log(\rho), \theta)$ are the log-polar coordinates transformed from the original (ξ, η) coordinates. The transformation is performed with the

$$\rho = R \cdot \sqrt{\xi^2 + \eta^2} \qquad (4)$$

and

$$\theta = tan^{-1}(\eta/\xi) \qquad (5)$$

expressions. The radial coordinate is scaled to half the size of the shorter edge of the frame in the log-polar transform with the coefficient C_R. This coefficient is needed to reconstruct the structure scaling factor f_s. The angular coordinate is upsampled to 360 pixels to get each pixel in the FMS to correspond to 1 degree (see Fig. 4 (e) and (f)).

3. *Example Fourier-Mellin transformation*

Eqn. 3 shows that the log-polar transformed FMS experiences a linear shift in the θ_0 and $\log(f_s)$ directions due to rotation and scaling, respectively. The scaling factor can be calculated by taking the exponent of the $\log(f_s)$ displacement. The Fourier-Mellin transformation steps described above are depicted in Fig. 4.

Fig. 4 (a) and (b) depict the FMSs of two consecutive frames around an ELM crash in shot #141319 (the raw frames are depicted in Fig. 1). The FMSs are calculated after zero-padding the pre-processed frames to avoid overlapping of the positive and negative wave number spectra[20]. A void is visible in the center of both spectra originating from the polynomial subtraction pre-processing step (described in detail in Sec. III B in Ref. 7). The translation invariance of the FMS and the angle difference between the two structures are both visible between Fig. 4 (a) and (b).

Fig. 4 (c) and (d) show the log-polar transformed FMSs (a) and (b), respectively. The angle difference is transformed into linear displacement in the vertical direction in the plots (notice the vertical displacement of a few peaks). The peaks are not displaced significantly in the horizontal direction meaning lack of scaling (expansion or contraction) between the two frames. It must be noted that typically the angle of rotation and the scaling factor cannot be directly read from the log-polar transformed FMSs and can only be estimated through calculation of the 2D CCCF (see Sec. II B 4).

4. *2D cross-correlation coefficient function (CCCF)*

The angle of rotation and the scaling factor can be estimated from the displacement of the maximum of the 2D CCCF[21] calculated between the two log-polar transformed FMSs. The 2D CCCF is calculated with the method described in Ref. 7. For the sake of completion, the definition of the CCCF function is repeated in the Appendix in Sec. A2. Before calculation of the 2D CCCF, the mean value of the FMS is subtracted from it because a constant offset introduces an unwanted bias in the calculation.

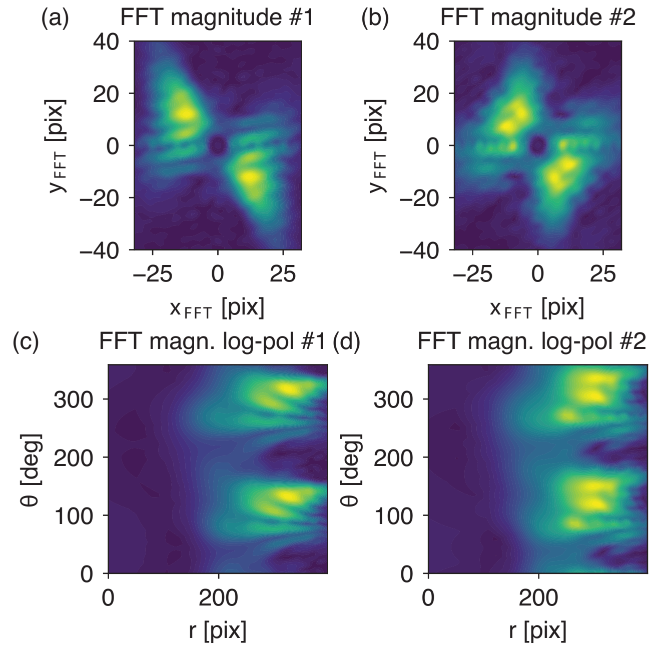

FIG. 4. Original and log-polar transformed Fourier magnitude spectra. (a,b): Fourier magnitude spectra of the pre-processed frames in Fig. 1 (a) and (b), respectively. (c,d): log-polar transformed (a) and (b) Fourier-magnitude spectra, respectively. 1

Fig. 5 depicts the 2D CCCF calculated between the two FMSs. In the upper right corner of the plot a small range around the origin is enlarged where one can see the displacement of the maximum from the origin. This indicates rotation in the negative, clockwise (CW) direction as well as slight displacement in the scaling direction (the displacement is highlighted with red lines). The x axis in the plot is the scaling pixel lag between the two log-pol transformed FMSs. The scaling factor f_s can be calculated from the horizontal pixel displacement, Δp, with the

$$f_s = e^{\frac{\Delta p}{x_{size,pol}/log(C_R)}} \qquad (6)$$

expression, where $x_{size,pol}$ is the size of the log-polar transformed FMS in the x direction, C_R is the radius of a circle in the center of the FMS within which the log-polar transform was performed. The value of C_R value was set to half of the horizontal frame size ($C_R = 32$ for the NSTX GPI). In principle the scaling factor could be used to characterize the size change of the filament. However, if the size of the structure changes differently in the poloidal and radial directions, the meaning of the expansion fraction is ambiguous therefore we do not discuss it further.

The position of the CCCF's maximum is found by fitting

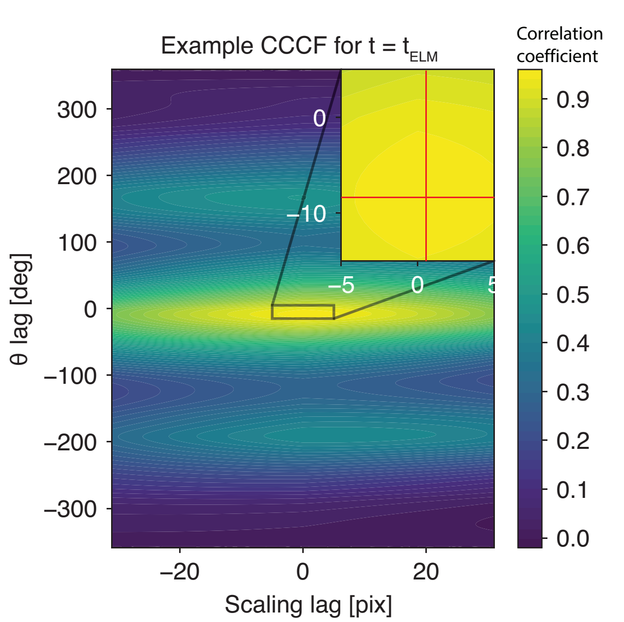

FIG. 5. The two-dimensional cross-correlation coefficient function calculated between the two log-polar transformed Fourier magnitude spectra in Fig. 4 (c) and (d). A small area around the maximum is enlarged in the upper right corner. The displacement of the maximum from the origin is highlighted with red lines here.

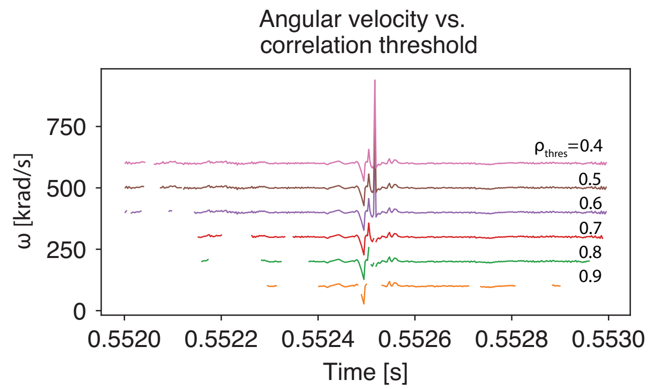

FIG. 6. Example angular velocity estimates for different correlation coefficient thresholds for shot 141319. The curves with different thresholds are offset by 100 krad/s with respect to the previous one. Based on these results, the correlation threshold was set to 0.7.

a 2D parabola onto the ±5pixel range around the pixel position of the maximum. This fitting process effectively increases the angular velocity and scaling factor resolution of the estimation. Finally, the position of the maximum is calculated analytically from the parameters of the fit parabola (for further details see Sec. III C 3 in Ref. 7. The angular velocity is calculated by dividing the estimated angle of rotation by the sampling time.

C. Post-processing

So far, no assumption was made on the shape of the structure or its position with respect to the measurement frame. In some cases the shape of the structure can change between frames so rapidly that the angle of rotation cannot be assessed. In other cases, the structure could either enter or exit the frame from one frame to another, which can also make estimating the angle of rotation uncertain. To tackle these issues, the calculation is considered invalid when the maximum of the 2D CCCF calculated between the pre-processed frames do not reach a certain value. The maximum of the 2D CCCF characterizes the similarity of the structure from one frame to another. The choice of the correlation threshold is based on a user defined acceptance level. To choose this value adequately, the results need to be plot against the different threshold values.

An example correlation threshold calculation can be seen Fig. 6. The thresholds were set between 0.4 and 1.0 with 0.1 increments. The curve with 1.0 is not visible because no points have 100% correlation. A large peak is visible for the curves $\rho_{thres} \leq 0.6$ (ρ_{thres} is the correlation threshold) which is due to the large shape change between the frames. Hence the correlation threshold was set to 0.7 in our application.

The value of the correlation threshold needs to be assessed for the particular application. Its choice is a compromise between keeping as many valid estimates as possible while filtering out the invalid ones. If the correlation threshold is set too high, too few valid estimates are returned. If it is set too low, invalid rotation events will also be considered as valid. The acceptance threshold could also be based on a different metric, however, assessment of it for further applications is up to the user and it is outside the scope of the paper.

D. Implementation of the method

The presented data analysis method is implemented in Python and can be found in the GitHub repository under Ref. 22 The implementation significantly relies on the NumPy[23], SciPy[16], scikit-image[18] and Matplotlib[24] python packages. The core of the method relies on the FLAP library[25] which facilitates analysis of large multidimensional data sets.

III. TESTING THE ANGLE OF ROTATION ESTIMATION METHOD WITH GAUSSIAN-STRUCTURES

In this section the results of the testing of the angle of rotation estimation method are shown. To test the method translating and rotating Gaussian-structures are generated with different rotation angles and elongations. The structures are generated for the typical size of the NSTX GPI measurement. Furthermore, the method is also tested for different square shaped frame sizes and relative noise levels, as well.

An example rotating and propagating Gaussian-structure is depicted in Fig. 7. The structure has an elongation of 2 and it is rotated by +15between Fig. 7 (a) and (b).

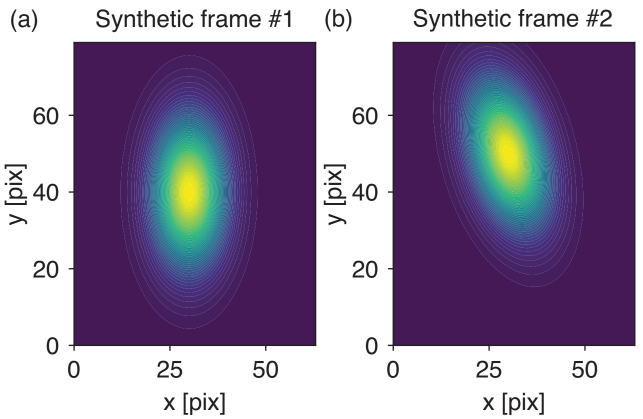

FIG. 7. Example synthetic frames of a rotating Gaussian-structure. (a) example Gaussian-structure; (b) the example Gaussian-structure rotated and displaced. The structure's shorter characteristic size is set to 15 pix while the longer is 30 pix, i.e., its elongation is 2. The structure is displaced by 10 pix in the y direction and rotated by +15between frames.

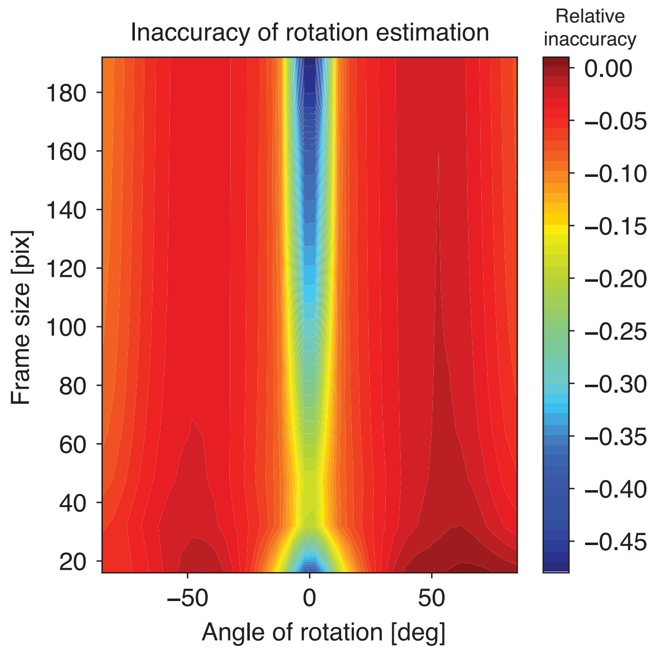

FIG. 8. Testing the angle of rotation estimation accuracy against the set angle of rotation (x axis) and the frame size (y axis). The contour levels show the relative inaccuracy of the angle estimation. (The relative inaccuracy is the ratio of the estimated minus the set angle, and the estimated angle.)

The Gaussian-structure can be propagated by a set number of pixels, rotated by a set angle of rotation, and expanded by a set percentage between frames. The full width at half maxima (FWHM) sets the size of the structure. The size of the frame and the relative noise level of the generated signal can be set, as well. No synthetic background signal is added to the synthetic signals. The testing solely focuses on the rotation estimation and thus, the scaling factor estimation is not tested for.

It must be noted that the shape of filaments in plasma experiments could be different from Gaussian (see, e.g., Fig. 3). The shape of the structure is translated into the log-polar Fourier magnitude spectrum. The displacement of the peaks in the CCCF calculated from the FMSs does not depend on the shape as long as it is relatively far from circular (see Fig. 9) and does not change significantly between frames. The shape of the structure needs to be resolved well enough to characterize its rotation accurately (see Fig. 8). The shape of the structure can change between frames in plasma experiments. If the shape changes rapidly, the imposed correlation threshold renders the analysis invalid for the corresponding frames. In these cases, the rotation of the filament is usually difficult to identify in the frames by eye, as well.

A. Testing the angle rotation estimation accuracy vs angle of rotation and the frame size

The proposed angle of rotation estimation method was first tested for its accuracy against the set angle of rotation of the Gaussian-structure and the size of the synthetic frame. The size of the structure in the x direction was fixed to 20% of the frame size. The elongation (ratio of the x and y FWHM of the Gaussian) of the Gaussian was set to 2 (i.e., 40% of the frame size). The smaller the frame size is, the smaller the number of pixels representing the structure, which ultimately influence the visible rotation angle. As a simple example, if the structure is only defined by 9 pixels, i.e., a 3 pix by 3 pix structure, the angle of rotation can only have a 360/8 pix=45pix^{-1} accuracy.

Although, the parabolic fit of the CCCF's peak increases the resolution of the estimation, a threshold for the frame size is expected under which the angle estimation will have high inaccuracy. The range of the angle of rotation was set to [-85,85]. Rotating the structure by ±90was avoided, because of the symmetry of the 2D Gaussian function and the ambiguity of its angle. Zero-degree rotation was not included in the calculation, because of the zero division in the relative inaccuracy calculation. The frame size was varied between 16 pix by 16 pix and 200 pix by 200 pix with increments of 16 pix in both x and y directions. The method was unable to produce accurate results for frames under the size of 16 pix by 16 pix, therefore, those calculations are not included in the results either. The results of the testing are depicted in Fig. 8.

Fig. 8 shows that the method can only give relatively accurate, <20% estimates of the angle of rotation for frame sizes between 30 pix and 80 pix for rotation angles lower than 10. For lower frame sizes, the interpolation of the log-polar transform introduces high inaccuracy, >20%. The lower the pixel count of a frame is, the lower the number of points which determine the angular coordinate of the log-polar transformation. Ultimately, this lowers the accuracy of the estimation in this method. The source of the increasing inaccuracy towards higher frame sizes at low angles is unknown and still under

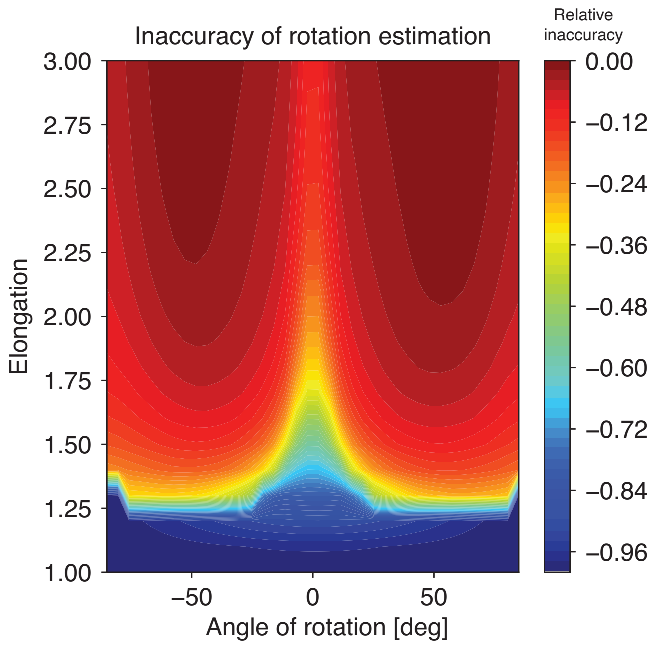

FIG. 9. Testing the angle of rotation estimation accuracy against set rotation angle (x axis) and elongation (y axis). The contour levels depict the relative inaccuracy of the estimation.

investigation.

The method can provide an estimate of the rotation angle for rotation angles higher than 10and frame sizes higher than 30 pix by 30 pix with lower than 10% relative accuracy which is acceptable for analysis of plasma filaments.

It must be noted that these results are representative only for rotating and propagating Gaussian-structures or structures which are close to Gaussian shaped (like most plasma filaments). For different applications, the accuracy of the method needs to be tested with differently shaped structures.

B. Testing the angle estimation accuracy vs set angle and elongation

In the next step the method is tested against differently elongated Gaussian-structures. The shorter FWHM of the structure is set to 20% of the 80 pix frame size (same as the longer frame size of the NSTX GPI diagnostic). Investigation of the elongation is important because the method cannot resolve the rotation of a circular structure (where the elongation equals one). Thus, in this testing step we also aim for finding the elongation threshold for Gaussian-structures above which the method can resolve rotation accurately. The rotation angle range of the test was set to the same as in Sec. III A. The elongation was set between 1.0 and 3.0 with 0.1 increments. The results of the test are shown in Fig. 9.

Fig. 9 shows that the method cannot estimate the angle of rotation for structures with 1.0 elongation, i.e., circular ones. For rotation angles below 10, the rotation can only be resolved with acceptable, $\sim 20\%$, accuracy at elongations higher than 2.0. For rotation angles higher than 10, the elongation can be as low as 1.5 to get accurate estimates of the rotation.

It must be noted that these limitations apply for low rotation angles, and more importantly to smooth Gaussian-structures. Rotation of structures with coarser intrinsic structures could possibly be estimated by the method with higher accuracy.

C. Testing the angle estimation accuracy vs noise

Imaging diagnostics are inherently noisy due to the statistical nature of photon emission. Furthermore, the detector and the detection electronics also introduce noise in the measurement. Therefore, it can be insightful to investigate the influence of noise to the angle of rotation estimation.

To simulate the measurement noise, random frames were generated with white noise with the noise amplitude set between [0, 2.0] with 0.1 increments to correspond to the relative noise level. Then the Gaussian synthetic signal was multiplied by the random frames and the result was added to the original frame. This step was performed for all of the generated synthetic frames. The Gaussian-structures were generated similarly to the previous ones, but their size was fixed to [10 pix, 20 pix] and the frame size was fixed to the NSTX GPI's [64 pix, 80 pix] frame size. No translational velocity was introduced to the structure. The analysis was repeated 25 times and the mean, and the standard deviation of the relative inaccuracy of the estimates were calculated.

The mean relative inaccuracy of the angular velocity estimation as a function of the angle of rotation and the relative noise level is depicted in Fig. 10 (a) and the standard deviation in 10 (b). The results show that the inaccuracy of the rotation angle estimate is close to independent from the relative noise level up to approximately 50% noise. The standard deviation of the inaccuracy starts increasing from 25% relative noise level for rotation angles in the range of [-10, 10]. These results show that the presented angular velocity estimation method is indeed robust against measurement noise.

IV. DISCUSSION

In this section we discuss the capabilities of the analysis method in plasma experiments. We apply the technique on a GPI measurement of an NSTX plasma regime exhibiting strong blob activity and another one where an ELM event is present.

A. Analysis of a blob event

An H-mode shot, No. #141307 was chosen for this analysis which exhibits strong blob activity in the time range around the peak of the GPI signal. Nine frames from the analyzed time range of the discharge are shown in Fig. 11. The blob is slowly propagating outwards and downwards in the ion diamagnetic direction while it is rotating in the negative clock-

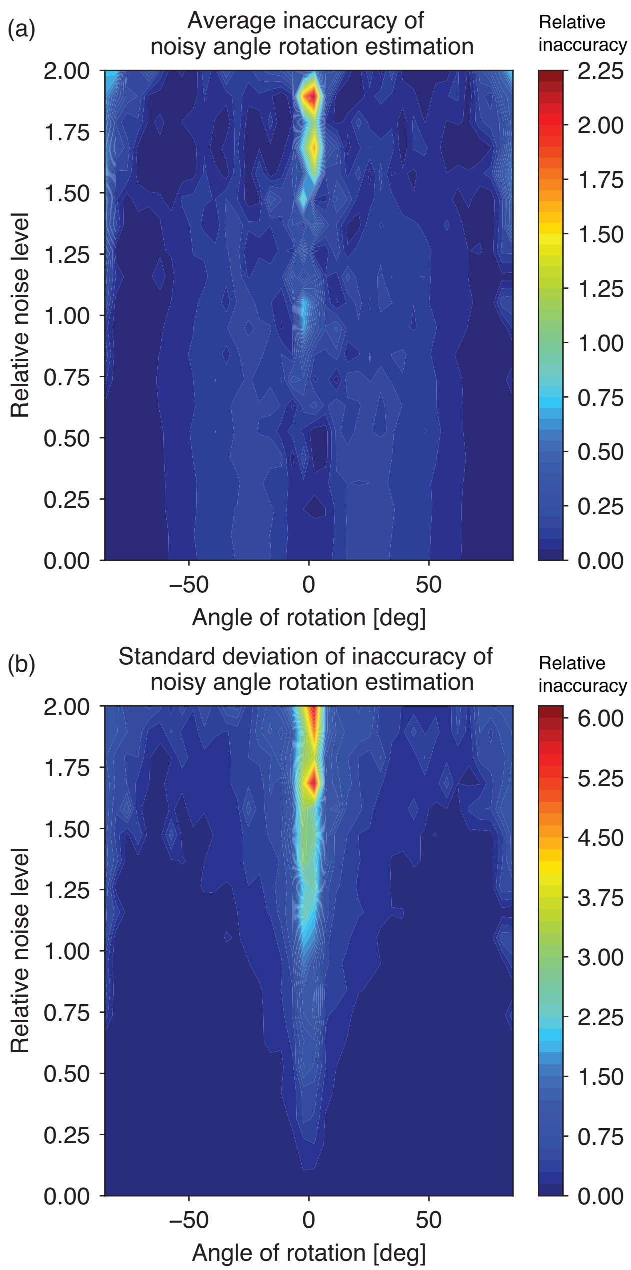

FIG. 10. Inaccuracy of the angle of rotation estimation method against white noise at a fixed frame and structure size. (a) Average relative inaccuracy of 25 random noise calculations; (b) Standard deviation of the inaccuracy of the 25 random noise calculations.

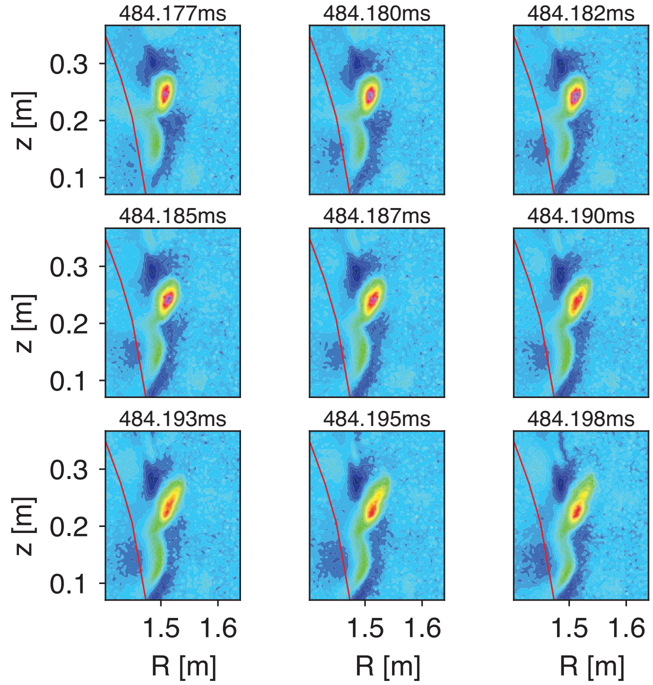

FIG. 11. Consecutive GPI frames of a blob event from an NSTX H-mode shot #141307. The first frame is the upper left one at t=484.177ms. Time evolves from left-to-right and then top-to-bottom row-by-row. The blob is slowly rotating in the clockwise direction while its shape is getting more elongated. The separatrix is depicted with a red curve in each frame.

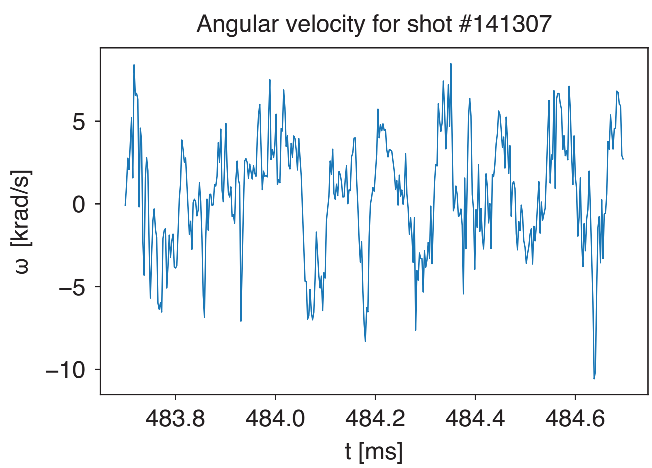

FIG. 12. Result of the angular velocity estimation for a time range with strong blob activity from the H-mode shot #141307.

wise direction. Its shape is getting elongated during its propagation.

The presented pre-processing steps were applied to the signal and the angular velocity was estimated for the analyzed time range with the presented angle of rotation estimation method. The results of the calculation are depicted in Fig. 12.

The analysis correctly identifies spinning in the negative, clockwise direction. The peak of the angular velocity is $\sim -8\mathrm{krad/s}$ in the time range. In fig. 12, there are time ranges where there is no estimated angular velocity. In these time ranges the peak correlation coefficient between the consecutive frames did not reach a threshold of $\rho_{\mathrm{thres}} = 0.7$.

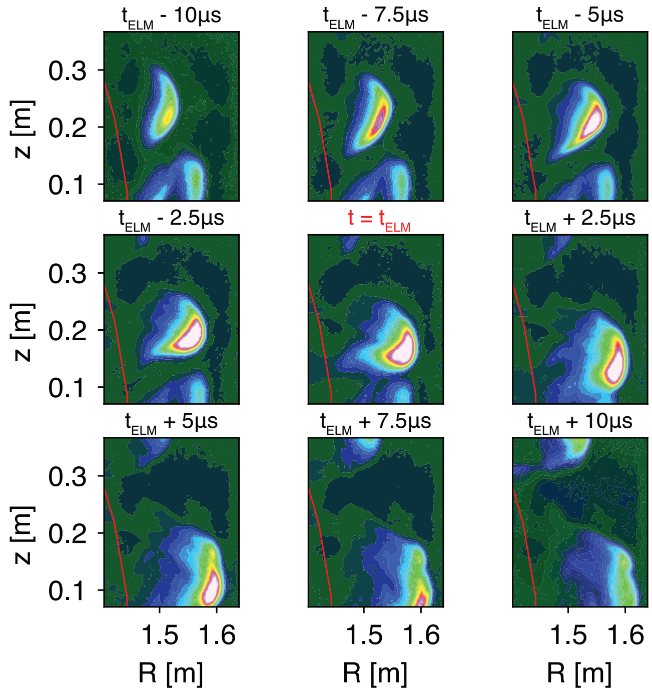

FIG. 13. Example frames of an NSTX ELM event measured by the GPI from shot #141319 clearly showing strong rotation, poloidal and radial propagation. The first frame is the upper left one at $t = t_{ELM} - 10\mu s$ where $t_{ELM} = 552.497$msec. Time evolves from left-to-right and then top-to-bottom row-by-row. The blob is slowly rotating in the clockwise direction while its shape is getting more elongated. The separatrix is depicted with a red curve in each frame.

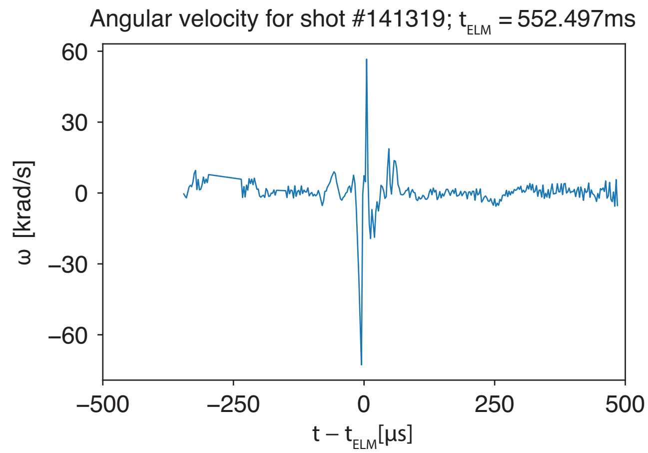

FIG. 14. Result of the angular velocity estimation for the ELM event at $t_{ELM} = 552.497$msec in shot #141319.

B. Analysis of an ELM filament

The presented angular velocity estimation method can be applied to edge localized mode filaments, as well. In fact, the observation of ELM filament rotation motivated the development of the presented angular velocity estimation analysis technique. Fig. 13 depicts an example ELM event where the rotation of the ELM filament is visible.

The presented method was applied to a 1 msec long time range around the ELM crash. The results of the analysis are depicted in Fig. 14.

The ELM filament clearly shows a spin-up effect in the negative clockwise direction, the ion gyro motion's direction, which reaches $\approx -60\mathrm{krad/s}$ at the time of the ELM crash, at $t = t_{ELM}$. The filament spins backwards in the counter-clockwise direction after the ELM crash after which it exits the frame of the measurement.

C. Comparison of the CCCF-based method to other means of angular velocity estimates

The angular velocity of filamentary structures can also be estimated by other analysis techniques. Most of these methods rely on identifying the structures one-by-one, fitting them with an ellipse or 2D Gaussian function frame-by-frame, and then the angular velocity can be estimated from the angle difference of tracked structures. A contour path segmentation and ellipse fitting based method is used in Ref. 11 by Zweben. We used a similar implementation in Ref. 6 to estimate the size and elongation of the ELM filaments. The same method was used to estimate the radial and poloidal velocities therein, but it was found that the results have too high uncertainty to be utilized for differential estimations such as the velocity. A different structure segmentation method was used by Farley in Ref. 26 which relies on the watershed segmentation[27] based technique and 2D Gaussian fitting of the segmented structures.

Both structure segmentation schemes were implemented in the Ref. 22 library[28]. The identified structures are tracked based on the overlap of the identified characterizing contour paths between the consecutive frames in both segmentation schemes. The identified and tracked structures can then be fit by an ellipse[29]. The angle of the ellipse can then be calculated from the fit parameters. Finally, the angular velocity can be calculated from the angle difference of the tracked structures divided by the sampling time. The structures can also be fit by a 2D Gaussian function, but this was found to be more uncertain because the spatial distribution of the filament light intensity was non-Gaussian in many cases. In the following paragraph we compare these methods to the presented CCCF based angular velocity estimation method. Discussion of further details of the structure identification and tracking algorithms are outside the scope of this paper.[30].

The contour and watershed segmentation-based angular velocity estimation techniques were applied to the same shots as the CCCF based method was, #141307 and #141319 and the results are depicted in Fig. 15 (a) and (b), respectively. The results calculated with the structure segmentation based methods show high noise which is not visible in the rotation of the filaments in the GPI signal. The reason for this high noise originates from a few contributing factors. These methods do not suppress the photon noise of the GPI measurement whereas the CCCF based method inherently does strong noise suppression. Furthermore, the identified characterizing con-

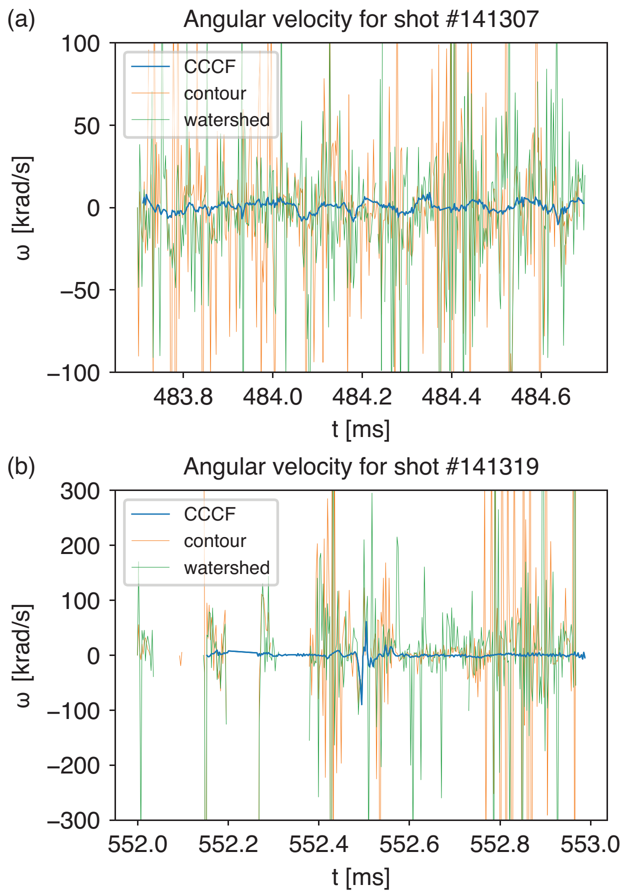

FIG. 15. Comparison of the CCCF based angular velocity estimation and the segmentation based techniques. (a) Comparison for the blobs in shot #141307; (b) Comparison for the ELM filament in shot #141319.

tour path could also be identified at a different intensity level and have a different shape and thus angle between two frames which also introduces uncertainty. Based on the comparison the CCCF based method is the better choice for analyzing frame-by-frame filament rotation imaged by GPI due to its robustness and noise tolerance.

D. Assumptions and limitations

It is important to discuss the assumptions made during the development of the angular velocity estimation method as well as the limitations of the analysis technique.

To get accurate estimates with the proposed method, it is imperative to remove the stationary background and offset from the signal. If the background is non-stationary, a time resolved background subtraction method needs to be implemented. The time scale of the background evolution needs to be at least an order of magnitude slower than the time scale of the analyzed phenomenon. In case of blobs, the background typically evolves on 10 msec time scale while blobs typically "evolve" on less than a 100 μs time scale (see bottom of Table 1 in Ref. 11). In case of ELM filaments, the background signal was found to be evolving on a 1 msec time scale while the ELM filament evolved on a few μs time scale. The separation of background and phenomenon time scales needs to be ensured for further applications.

The core of the presented method, the Fourier-Mellin transform was originally developed for image registration where the shape of the imaged structures does not change between frames and only zooming in or out is expected. Our method was applied on images where the shape of the structure could significantly change between frames. To prevent significant shape change to be taken as false rotation, a threshold was imposed on the cross-correlation coefficient calculated between the pre-processed frames. The optimal correlation threshold was found to be 0.7 for the presented application on plasma filaments measured with gas-puff imaging.

The presented method can estimate the characterizing angular velocity for a relatively large region-of-interest (ROI). The size of this ROI must be at least 30 pix by 30 pix (see Sec. III A). If only a single structure is present in the frame, such as the ELM filament after the ELM crash[6], the method accurately estimates the angular velocity. Blobs on the other hand can be present more than one at a time in the frame of the measurement. Should there be more than a single structure present in the frame, the estimated angular velocity would be a weight averaged one where the weights are the average integrated intensities of the structures.

The presented plasma measurement analyses utilized the entire frame of measurement to estimate the angular velocity of the ELM filament and the blobs. One could ask whether constraining the analysis to a smaller ROI would influence the outcome. In principle one could choose a ROI which enclosed the analyzed structure only, however, that would require the perimeter of the structure to be identified which would make the analysis technique less robust. If the same, but smaller than frame size ROI was used for the analysis, the number of valid points in the results would be reduced because the structure would be outside the ROI for a larger portion of the time series. If the structure is not propagating to certain areas of the frame at all (e.g., to a column of pixels imaged outside the limiter shadow) one could reduce the analyzed frame size to speed up the analysis.

Analysis of rotation in imaging measurements is limited to structures with circular symmetry. Since our method was developed to analyze imaging data, it cannot resolve the rotation of a circular structure or a structure close to circular. Most of the observed filaments are elongated poloidally which makes the angular velocity estimation method viable for their analysis.

Finally, it must be noted that the presented method can only be utilized if the sensitivities of the pixels are equal, or they have been calibrated. This needs to be performed before any of the analysis steps can be done.

V. SUMMARY

Filamentary structures are responsible for significant amount of heat and particle transport in fusion plasmas. Blob filaments are ubiquitous to the background turbulence in edge and SOL plasmas and ELM filaments could cause irreversible damage to the plasma facing components and they degrade plasma confinement, as well. The dynamics (rotation and translation) of these filaments partially determine their effects on the plasma facing components, therefore, understanding their physics is important for the future of fusion energy production.

In this paper we present a novel method for estimating the angular velocity of plasma filaments measured by 2D imaging diagnostics. After pre-processing the signal, the two-dimensional spatial Fourier spectrum of each frame is calculated. Then the Fourier magnitude spectra are calculated which is log-polar transformed hereafter. Finally, the angle of rotation can be estimated from the displacement of the maximum of the 2D cross-correlation coefficient function from the origin in the angular coordinate's direction.

To assess the limitations of the proposed method, it was tested with rotating and displaced Gaussian-structures at different structure elongations, angle of rotations, measurement frame sizes and relative noise levels. It was found that the method can accurately estimate the angle of rotation for structures with elongation of at least 1.5 for rotation angles over 10and elongation of at least 2.0 for rotation angles under 10. The method was found to be capable of accurately estimating the rotation angles for frame sizes higher than 30pix by 30pix. The noise assessment results show that the proposed method is robust against noise, the inaccuracy of the method is noise independent at least up to 25% relative noise level for a fixed structure and frame size.

The method was applied to GPI measurements of plasma filaments in the NSTX. Estimation of the angular velocity of blobs revealed their change of spinning direction during their propagation. Applying the analysis method on an ELM filament event revealed that the filament spins up significantly in the ion gyro motion's direction during the ELM crash. The method was compared to contour and watershed structure segmentation based angular velocity estimation methods by applying them on the same GPI measurements of blobs and ELM filaments. The presented method was found to be more robust and less uncertain than the segmentation-based methods.

In summary we have developed a robust and relatively accurate angular velocity estimation method which can characterize the rotation of propagating filamentary structures. In the future the method will be used to assess rotation of blobs in a large database. Furthermore, the technique will also be applied to characterize the motion of disruption mitigation shattered pellets[31].

ACKNOWLEDGMENTS

The authors thank the fruitful discussions with Jim Myra during our collaboration on ELM filament rotation. This work was supported by U.S. DOE Contract No. DE-AC02-09CH11466 (PPPL).

AUTHOR DECLARATIONS

Conflict of interest

The authors have no conflict of interest to disclose.

Data availability

The data that support the findings of this study are openly available under Ref. 32 [to be changed before the final submission].

Appendices

A1. PROOF OF THE FOURIER MAGNITUDE SPECTRUM ROTATION EXPRESSION

The following derivation shows the details of the Fourier magnitude spectrum based angular velocity estimation method described in Sec. II.

If one introduces rotation between frames f_1 and f_2 and calculates their Fourier-spectra, then the two spectra are related by

$$F_2(\xi,\eta) = c(x_0,y_0)\cdot F_1(\xi\, cos(\theta_0)+\eta\, sin(\theta_0), -\xi\, sin(\theta_0)+\eta\, cos(\theta_0)) \tag{A1}$$

If rotation and translation are both introduced between frame f_1 and f_2 as shown in equation

$$f_2(x,y) = f_1(x\, cos(\theta_0)+y\, sin(\theta_0)-x_0, -x\, sin(\theta_0)+y\, cos(\theta_0)-y_0) \tag{A2}$$

,

then one can show that their Fourier magnitude spectra are related by

$$M_2(\xi,\eta) = \cdot M_1(\xi\, cos(\theta_0)+\eta\, sin(\theta_0), -\xi\, sin(\theta_0)+\eta\, cos(\theta_0)) \tag{A3}$$

If the magnitude spectra are transformed into polar coordinates (ρ,θ), this relationship can be written in the form of

$$M_1(\rho,\theta) = M_2(\rho,\theta-\theta_0) \tag{A4}$$

.

meaning that if there is translation and rotation introduced between two consecutive frames, their polar transformed magnitude spectra are related by a linear displacement in the angle coordinate.

The calculations so far have assumed scale-invariance between the structures in the frames. However, as seen in Ref. 6, the ELM filament's size is evolving during the crash. In the zeroth order, the filament's size evolution can be characterized by a single scaling factor. It can be shown that if translation, rotation, and linear scaling is introduced between two frames, their Fourier magnitude spectra are related by

$$M_1(\rho,\theta) = M_2(\rho/f_s, \theta-\theta_0) \quad \text{(A5)}$$

where $\mathrm{f_s}$ is the scaling factor in both x and y directions. The division with the scaling factor can be transformed into displacement if log-polar transformation is used instead of the polar transform. Equation

$$M_1(log(\rho),\theta) = M_2(log(\rho)-log(f_s), \theta-\theta_{f_s}) \quad \text{(A6)}$$

transforms the division into displacement. This expression is similar to Eqn. 2 where the linear displacement was found by calculating the 2D spatial CCCF between the consecutive frames. One can utilize the same method on the log-polar transformed 2D Fourier magnitude spectra to estimate the rotation and the scaling evolution of the ELM filament during the ELM crash.

A2. TWO-DIMENSIONAL SPATIAL CROSS-CORRELATION COEFFICIENT FUNCTION [7]

.

The angular velocity estimation method relies on the calculation of the 2D spatial cross-correlation coefficient function, hence, we repeat it's definition for completeness. Its definition is given by

$$\rho_{a,b}(\kappa_x,\kappa_y) = \frac{R_{f_{a,b}}(\kappa_x,\kappa_y)}{\sqrt{R_{f_a,f_a}(0,0)}\cdot\sqrt{R_{f_b,f_b}(0,0)}}, \quad \text{(A7)}$$

where $\rho_{(\mathrm{f_a},\mathrm{f_b})}(\kappa_x,\kappa_y)$ is the 2D spatial cross-correlation coefficient function at spatial displacement κ_x and κ_y in the x and y direction, respectively. $\mathrm{R_{a,b}}$ is the spatial cross-correlation function estimate between the temporally consecutive frames $\mathrm{f_a}$ and $\mathrm{f_b}$ given by Eqn. A8. $\mathrm{R_{f_a,f_a}}(0,0)$ and $\mathrm{R_{f_b,f_b}}(0,0)$ are the 2D spatial auto-correlation function estimates of frame $\mathrm{f_a}$ and $\mathrm{f_b}$, respectively, given by Eqn. A8 at $\kappa_\mathrm{x}=0$ and $\kappa_\mathrm{y}=0$. The 2D spatial cross-correlation function can be written as

$$R_{a,b}(\kappa_x,\kappa_y) = C_{\kappa_x,\kappa_y}\cdot\sum_{i,j} f_a(x_i-\kappa_x, y_j-\kappa_y)\cdot f_b(x_i,y_j), \quad \text{(A8)}$$

where $\mathrm{i}=0...\mathrm{N_x}$ and $\mathrm{j}=0...\mathrm{N_y}$ (i.e., summation for all pixels), where $\mathrm{N_x}$ and $\mathrm{N_y}$ are the number of pixels in the x and y direction, respectively. $\mathrm{C}_{\kappa_\mathrm{x},\kappa_\mathrm{y}}$ is a normalization factor and equals the reciprocal of the overlapping number of pixels. Further discussion of the 2D CCCF and the way it can be calculated efficiently is discussed in Ref. 7.

[1] A. Kirk, H. R. Wilson, G. F. Counsell, R. Akers, E. Arends, S. C. Cowley, J. Dowling, B. Lloyd, M. Price, and M. Walsh (MAST Team), "Spatial and temporal structure of Edge-Localized Modes," Phys. Rev. Lett. **92**, 245002 (2004).

[2] D. A. D'Ippolito, J. R. Myra, and S. J. Zweben, "Convective transport by intermittent blob-filaments: Comparison of theory and experiment," Physics of Plasmas **18**, 060501 (2011).

[3] C. Ham, A. Kirk, S. Pamela, and H. Wilson, "Filamentary plasma eruptions and their control on the route to fusion energy," Nature Reviews Physics **2**, 159–167 (2020).

[4] A. Loarte, G. Saibene, R. Sartori, D. Campbell, M. Becoulet, L. Horton, T. Eich, A. Herrmann, G. Matthews, N. Asakura, A. Chankin, A. Leonard, G. Porter, G. Federici, G. Janeschitz, M. Shimada, and M. Sugihara, "Characteristics of type I ELM energy and particle losses in existing devices and their extrapolation to ITER," Plasma Physics and Controlled Fusion **45**, 1549–1569 (2003).

[5] T. Eich, B. Sieglin, A. Thornton, M. Faitsch, A. Kirk, A. Herrmann, and W. Suttrop, "ELM divertor peak energy fluence scaling to ITER with data from JET, MAST and ASDEX upgrade," Nuclear Materials and Energy **12**, 84 – 90 (2017), proceedings of the 22nd International Conference on Plasma Surface Interactions 2016, 22nd PSI.

[6] M. Lampert, A. Diallo, J. R. Myra, and S. J. Zweben, "Dynamics of filaments during the edge-localized mode crash on NSTX," Physics of Plasmas **28**, 022304 (2021).

[7] M. Lampert, A. Diallo, and S. J. Zweben, "Novel 2D velocity estimation method for large transient events in plasmas," Review of Scientific Instruments **92**, 083508 (2021).

[8] S. Derrode and F. Ghorbel, "Robust and efficient Fourier-Mellin transform approximations for invariant grey-level image description and reconstruction," Computer Vision and Image Understanding **83**, 57–78 (2001).

[9] X. Guo, Z. Xu, Y. Lu, and Y. Pang, "An application of Fourier-Mellin transform in image registration," in *The 5th International Conference on Computer and Information Technology* (2005) pp. 619–623.

[10] C. A. Wilson and J. A. Theriot, "A correlation-based approach to calculate rotation and translation of moving cells," IEEE Transactions on Image Processing **15**, 1939–1951 (2006).

[11] S. J. Zweben, J. R. Myra, W. M. Davis, D. A. D'Ippolito, T. K. Gray, S. M. Kaye, B. P. LeBlanc, R. J. Maqueda, D. A. Russell, and D. P. S. and, "Blob structure and motion in the edge and SOL of NSTX," Plasma Physics and Controlled Fusion **58**, 044007 (2016).

[12] M. Lampert, A. Diallo, J. R. Myra, and S. J. Zweben, "Internal rotation of ELM filaments on NSTX," Physics of Plasmas **29**, 102502 (2022).

[13] S. J. Zweben, J. L. Terry, D. P. Stotler, and R. J. Maqueda, "Invited review article: Gas puff imaging diagnostics of edge plasma turbulence in magnetic fusion devices," Review of Scientific Instruments **88**, 041101 (2017).

[14] S. J. Zweben, D. P. Stotler, F. Scotti, and J. R. Myra, "Two-dimensional turbulence cross-correlation functions in the edge of NSTX," Physics of Plasmas **24**, 102509 (2017).

[15] M. Ono, S. Kaye, Y.-K. Peng, G. Barnes, W. Blanchard, M. Carter, J. Chrzanowski, L. Dudek, R. Ewig, D. Gates, R. Hatcher, T. Jarboe, S. Jardin, D. Johnson, R. Kaita, M. Kalish, C. Kessel, H. Kugel, R. Maingi, R. Majeski, J. Manickam, B. McCormack, J. Menard, D. Mueller, B. Nelson, B. Nelson, C. Neumeyer, G. Oliaro, F. Paoletti, R. Parsells, E. Perry, N. Pomphrey, S. Ramakrishnan, R. Raman, G. Rewoldt, J. Robinson, A. Roquemore, P. Ryan, S. Sabbagh, D. Swain, E. Synakowski, M. Viola, M. Williams, J. Wilson, and N. Team, "Exploration of spherical torus physics in the NSTX device," Nuclear Fusion **40**, 557–561 (2000).

[16] P. Virtanen, R. Gommers, T. E. Oliphant, M. Haberland, T. Reddy, D. Cournapeau, E. Burovski, P. Peterson, W. Weckesser, J. Bright, S. J. van der Walt, M. Brett, J. Wilson, K. J. Millman, N. Mayorov, A. R. J. Nelson, E. Jones, R. Kern, E. Larson, C. J. Carey, İ. Polat, Y. Feng,

E. W. Moore, J. VanderPlas, D. Laxalde, J. Perktold, R. Cimrman, I. Henriksen, E. A. Quintero, C. R. Harris, A. M. Archibald, A. H. Ribeiro, F. Pedregosa, P. van Mulbregt, and SciPy 1.0 Contributors, "SciPy 1.0: Fundamental Algorithms for Scientific Computing in Python," Nature Methods **17**, 261–272 (2020).

[17] L. Assirati, N. R. Silva, L. Berton, A. A. Lopes, and O. M. Bruno, "Performing edge detection by Difference of Gaussians using q-Gaussian kernels," Journal of Physics: Conference Series **490**, 012020 (2014).

[18] S. Van der Walt, J. L. Schönberger, J. Nunez-Iglesias, F. Boulogne, J. D. Warner, N. Yager, E. Gouillart, and T. Yu, "scikit-image: image processing in python," PeerJ **2**, e453 (2014).

[19] B. Reddy and B. Chatterji, "An FFT-based technique for translation, rotation, and scale-invariant image registration," IEEE Transactions on Image Processing **5**, 1266–1271 (1996).

[20] Zero-padding is a process where the original frame is padded around with pixels having zero intensity. The resulting frame is typically three times larger than the original in both x and y directions because the padding is done with the same frame size as the original.

[21] The cross-correlation function (CCF), which researchers usually refer to, is not normalized with the zero-lag value of the auto-correlation function. The word coefficient in CCCF represents this normalization, where the original CCF is normalized to the range between [-1,1] and hence becomes the cross-correlation coefficient function.

[22] M. Lampert, "FLAP: Fusion Library of Analysis Programs, NSTX repository," `https://github.com/fusion-flap/flap_nstx/tree/RSI_2022_version`.

[23] C. R. Harris, K. J. Millman, S. J. van der Walt, R. Gommers, P. Virtanen, D. Cournapeau, E. Wieser, J. Taylor, S. Berg, N. J. Smith, R. Kern, M. Picus, S. Hoyer, M. H. van Kerkwijk, M. Brett, A. Haldane, J. F. del Río, M. Wiebe, P. Peterson, P. Gérard-Marchant, K. Sheppard, T. Reddy, W. Weckesser, H. Abbasi, C. Gohlke, and T. E. Oliphant, "Array programming with NumPy," Nature **585**, 357–362 (2020).

[24] J. D. Hunter, "Matplotlib: A 2D graphics environment," Computing in Science & Engineering **9**, 90–95 (2007).

[25] S. Zoletnik and M. Lampert, "FLAP: Fusion Library of Analysis Programs," `https://github.com/fusion-flap/flap`.

[26] T. Farley, N. R. Walkden, F. Militello, M. Sanna, J. Young, S. S. Silburn, J. Harrison, L. Kogan, I. Lupelli, S. S. Henderson, A. Kirk, and J. W. Bradley, "Filament identification in wide-angle high speed imaging of the mega amp spherical tokamak," Review of Scientific Instruments **90**, 093502 (2019).

[27] L. Najman and M. Schmitt, "Watershed of a continuous function," Signal Processing **38**, 99–112 (1994).

[28] The gpi/structure_segmentation.py file contains both the contour-based and the the watershed-based structure identification technique implementations in the FLAP_NSTX GitHub library under Ref. 22.

[29] R. Haloy and J. Flusser, "Numerically stable direct least squares fitting of ellipses," Sixth International Conference in Central Europe on Computer Graphics and Visualization , 125–132 (1998).

[30] The details of the segmentation algorithms can be found in the code on GitHub under Ref. 22 in gpi/structure_segmentation.py, while the tracking algorithm is implemented in gpi/analyze_gpi_structures.py. The details of these algorithms will be assessed in a future publication along with characterization of the structure shapes in GPI measurements.

[31] T. Gebhart, L. Baylor, M. Ericson, S. Meitner, A. Qualls, and D. Rasmussen, "Recent progress in shattered pellet injection technology in support of the ITER disruption mitigation system," Nuclear Fusion **61**, 106007 (2021).

[32] M. Lampert, A. Diallo, and S. Zweben, "Novel angular velocity estimation technique for plasma filaments data," `https://dataspace.princeton.edu/handle/88435/dsp011v53k0334` (2022).